Supporting Information for: Signatures of a two-dimensional ferromagnetic electron gas at the $La_{0.7}Sr_{0.3}MnO_3/SrTiO_3$ interface arising from magnetic reconstruction

N. M. Nemes,[1,2] M. J. Calderón,[3,2] J.I. Beltrán,[1,3] F. Y. Bruno,[1,2] J. García-Barriocanal,[1,2] Z. Sefrioui,[1,2] C. León,[1,2] M. García-Hernández,[3,2] M. C. Muñoz,[3] L. Brey,[3,2] and J. Santamaría[1,2]

[1] *GFMC, Departamento de Fisica Aplicada III, Universidad Complutense de Madrid, Campus Moncloa, E-28040 Madrid, Spain*
[2] *Unidad Asociada UCM-ICMM (CSIC)*
[3] *Instituto de Ciencia de Materiales de Madrid, ICMM-CSIC, Cantoblanco, E-28049 Madrid (Spain)*

(Dated: August 29, 2014)

The LSMO/STO multilayers exhibit temperature and field dependent resistivity and magnetism reminiscent of LSMO. However, there are important differences. In this report the focus is on the low temperature behavior of the angular dependence of the magnetoresistance. Overall, the resistivity is suppressed by magnetic field, a vestige of the colossal magnetoresistance (CMR) effect of LSMO.

I. EXPERIMENT

A. The LSMO/STO interface

The (001) oriented structure of perovskite oxides with general formula ABO_3 (CDO_3) consists of alternating AO (CO) and BO_2 (DO_2) planes, where A (C) is the rare earth and B (D) the transition metal. When two materials ABO_3 and CDO_3 are combined to form a heterostructure there are two possible interface configurations: AO-BO_2-DO and AO-CO_2-DO. In the present case the combination of LSMO and STO will render either a MnO_2-$La_{0.7}Sr_{0.3}O$-TiO_2-SrO (type I) or a $La_{0.7}Sr_{0.3}O$-MnO_2-SrO-TiO_2 interface (type II). When growing the first LSMO layer of the superlattice in a TiO_2 terminated STO substrate the interface will always be type I. However when growing the first STO layer on top of LSMO both interface types are possible[1].

It has been shown that in samples grown by pulsed laser deposition the termination layer of LSMO grown on top of TiO_2 terminated STO depends on the oxygen pressure during growth. At low pressures the layer is terminated in a MnO_2 plane while higher pressures seem to favour a $La_{0.7}Sr_{0.3}O$ termination layer[2]. This will allow for the deposition of a subsequent STO layer with either type of interface. In fact very recently it has been shown that the LSMO-STO interface can be engineered by the insertion of different layers[3,4]. These examples show that the interface type might be tailored at will since it is a consequence of the deposition conditions that finally determine a kinetic vs thermodynamic control of the growth. The high oxygen pressure during the growth of our samples yields very thermalized growth at slow rate of deposition ($\sim$ 1 nm/min) and we have observed that the interfaces in the LSMO-STO superlattices are always type I ($La_{0.7}Sr_{0.3}O$-TiO_2)[5], although roughness develops as growth continues and interface type determination for the last few interfaces is less conclusive. We have also observed symmetric top and bottom interfaces for other systems: in $LaMnO_3$-STO superlattices both interfaces are LaO-TiO_2 [6]; in $La_{0.7}Ca_{0.3}MnO_3$-$YBa_2Cu_3O_7$ superlattices both interfaces are CuO_2-BaO-MnO_2 [7]; in the YBCO/STO system [8] both interfaces are CuO_2-BaO-TiO_2; and in $(Y_2O_3)_x(ZrO_2)_{1-x}$/STO superlattices[9] the termination layer of STO is always a TiO_2 plane. We believe that in the high oxygen pressure used for deposition the thermodynamic stability of the surface has a predominant role in determining the interface type. Hence, even in the absence of real-time in situ monitoring tools like RHEED, we routinely and reproducibly obtain symmetric interfaces in our heterostructures.

B. Transport measurements

In this section we first give the resistance and magnetoresistance data corresponding to the samples studied in the main paper. Figure 1 shows the temperature dependence of the superlattices and thin films that appear in Figure 2 of the main paper. The figure presents raw resistance values, not normalized in any way. The geometry for each sample was a van der Pauw arrangement with four contacts in the four squares of the 5*5 mm^2 square-shaped samples. The corresponding resistivities, the limiting low temperature values, are indicated as the abscissa of the inset to Figure 2. The color-coding in Fig. 1 corresponds to that in Fig. 2 of the main paper and its inset. Figure 1 also shows the resistance in a $B = 14$ T magnetic field applied perpendicular to the surfaces (interfaces) of the superlattices. For the LSMO thin films only the zero field resistance is shown. The resistance of the samples, superlattices as well as thin films, behaves essentially as that of canonic LSMO thin films. The thinner the films, the lower the Curie temperature and higher the resistivity. As discussed in Ref 5, superlattices with thin (2 unit cells) STO barriers behave like correspondingly thick LSMO films, all the constituent LSMO films couple together electrically and magnetically through the thin STO. Superlattices with thick (6 unit cells) STO barrier behave like individual thin LSMO films. The magnetoresistance of the samples at 10 K, with the magnetic field applied perpendicular to the surface, is shown in Figure 3. Again, superlattices with thick STO barriers give larger magnetoresistance than those with thin-

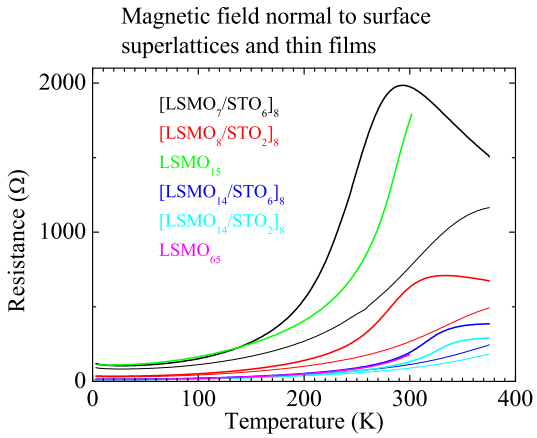

FIG. 1: (Color online) Resistance of $[LSMO_m/STO_n]_8$ superlattices and LSMO thin films in 0 (thick lines) and 14 T (thin lines) magnetic fields, applied perpendicular to the surface.

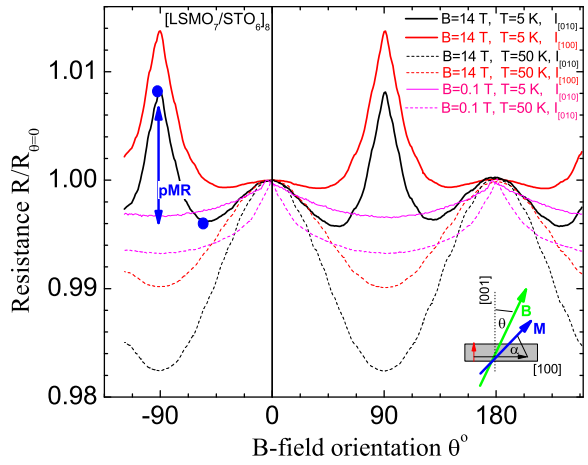

FIG. 2: (Color online) Angular MR for a $[LSMO_7/STO_6]_8$ multilayer with the magnetic field rotating θ away from the perpendicular [001] direction in the [001]/[010] plane, either staying perpendicular to the current ($I_{[100]}$), or rotating with respect to it ($I_{[010]}$). Rotations are shown in high field, B=14 T, at T=5 K with $I_{[010]}$ (thick black) and $I_{[100]}$ (thick red), and at T=50 K with $I_{[010]}$ (dashed black) and $I_{[100]}$ (dashed red), and in low field, B=0.1 T, with $I_{[010]}$, at T=5 K (magenta) and T=50 K (dashed magenta). The blue dots and arrow show the definition of pMR described in the text.

ner STO, for the same LSMO film thickness. The thicker the LSMO, the lower the magnetoresistance. Note that these curves do not show the colossal magnetoresistance expected near the metal insulator transition temperature around 300-350 K. The fact that there is considerable magnetoresistance remaining at low temperature in superlattices with thin LSMO (and thick STO) actually indicates hindered magnetic disorder, as discussed in Ref. 5.

Figure 4 highlights the characteristic resistance min-

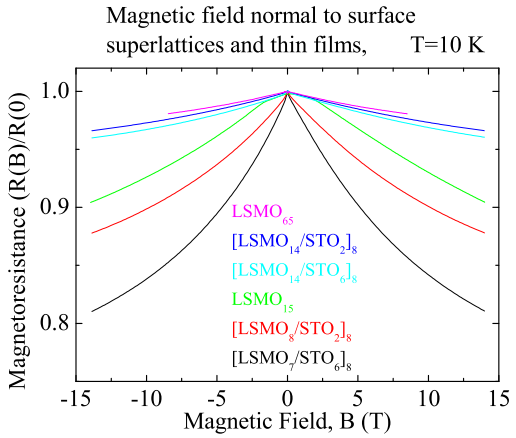

FIG. 3: (Color online) Magnetoresistance of $[LSMO_m/STO_n]_8$ superlattices and LSMO thin films at $T = 10$ K, with the magnetic field applied perpendicular to the surface of the films.

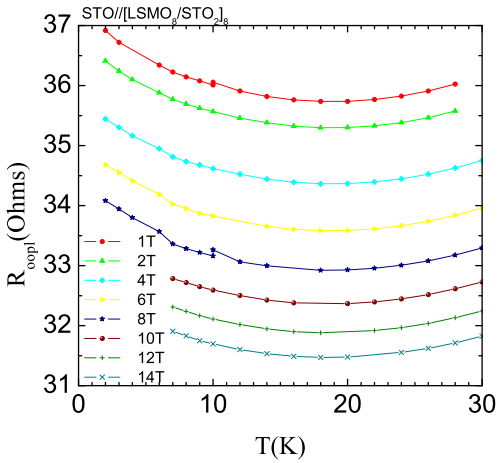

FIG. 4: (Color online) Low temperature resistance of a $[LSMO_8/STO_2]_8$ multilayer in several magnetic fields.

imum observed in manganite thin films[10]. Its effect is observed in Figure 6, where the angular MR curves show an overall nonmonotonic displacement. Importantly though, they do not cross for any temperature or magnetic field. This is to say that for any orientation of the magnetic field, plots similar to Figure 4 would be obtained.

We have performed transport measurements on manganite multilayers as a function of the angle between an applied magnetic field and the interfacial plane. The anisotropic magnetoresistance (AMR) in manganite films is typically measured by rotating the magnetic field in the film plane[11] but here the magnetic field is rotated out of plane. In out-of-plane rotations in high applied magnetic fields, such as the thick black or red lines in Fig. 2, an unexpected sharp peak appears along the in-plane direction

($\theta = 90^o$), which we call the in-plane angular magnetoresistance (pMR) peak. To see how unusual it is, let us first consider the expected behaviour.

Figure 2 gives a taste of the angular MR displayed by the multilayers at various temperatures and fields. At elevated temperatures the multilayers, similarly to manganite monolayers, show AMR where the additional MR is determined by the fraction of magnetization out of the film plane. In high fields therefore, where the magnetization follows the magnetic field, the curve follows a $\sin^2(\alpha)$ dependence (dashed lines in 14 T and 50 K), where $\alpha \sim 90^o - \theta$ is the angle between current and magnetization (see inset of Fig. 2). In low fields (magenta lines, in 0.1 T and 5 K or 50 K), the shape anisotropy of the film forces the magnetization towards the plane. Since $90^o - \theta$ is the angle between current and magnetic field, and not magnetization, the angular dependence is distorted, peaking sharply perpendicular to the film (0° and 180°), where the magnetization eventually is turned away from the plane (see inset of Fig. 2).

AMR in ferromagnets is sensitive to the relative angle between the current and the magnetic field. For the out-of-plane measurements, the magnetic field is always rotated within the [001] − [010] plane, along the [100] axis, but the current is measured both in the [010] ($I_{[010]}$ geometry) and in the [100] ($I_{[100]}$) directions. When the current is in the $I_{[010]}$ geometry, the angle between the magnetic field (and thus magnetization) and the current is given by $90^o - \theta$. But when the current is in the $I_{[100]}$ geometry, the magnetic field and the current are always perpendicular. In spite of this crucial difference for AMR, both configurations give the pMR-peak, emphasizing its origin in the band structure (see Sec. II A for the theoretical discussion).

When the magnetic field is rotated *in the plane of the interfaces* (Fig. 5) the characteristic $\cos^2(\phi)$ dependence of the AMR is observed as the angle between magnetization (following the magnetic field) and current is changed, up to the largest available magnetic fields (14 T) and lowest temperatures (2 K).

Figure 6 shows the angular MR for the $[LSMO_8/STO_2]_8$ multilayer in a magnetic field of 8 T in both current configurations $I_{[010]}$ and $I_{[100]}$. This figure illustrates how the pMR-peak arises as temperature is decreased in a strong magnetic field. Above 18-20 K the rotations maintain a typical AMR shape of $\cos(\theta)^2$, with the overall resistance decreasing with decreasing temperature. However, below this temperature, a sharp peak develops along the in-plane direction of the magnetic field. The resistance also starts to rise again near this temperature.

Fig. 7 shows the angular MR for the $[LSMO_8/STO_2]_8$ multilayer at high temperature (T=100K) and different magnetic fields. Here the pMR-peak does not appear, and only a more standard angular magnetoresistance with out-of-plane maxima remains. These maxima follow $\sim \cos^2(\theta)$ once the magnetization is saturated (above $\sim$ 2 T). The corresponding anisotropic MR amplitude is

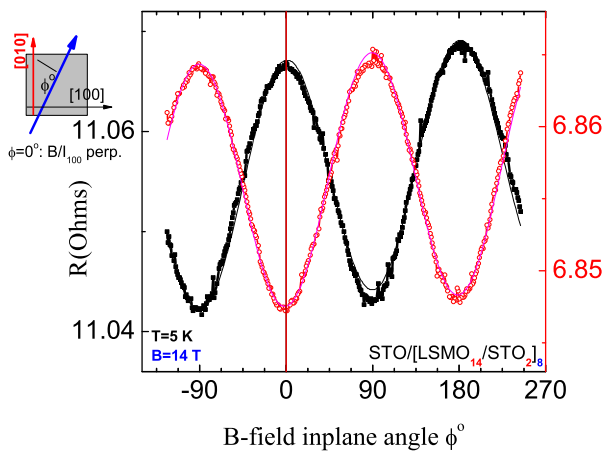

FIG. 5: (Color online) Angular MR with the magnetic field rotating ϕ away from [010] in-plane in the [010]/[100] plane, of a $[LSMO_{14}/STO_2]_8$ multilayer at T=5 K and B=14 T. The two current geometries are depicted in the inset with resistance data for $I_{[100]}$ shown with black squares and for $I_{[010]}$ with red open circles. The corresponding lines are sinusoidal fits.

independent of field and its magnitude is $\sim$ 2%. For lower fields, the magnetization is not aligned to the applied field, the curves are distorted and the angular MR tends toward a $|\cos(\theta)|$ shape. Overall the curves are shifted to lower resistance with increasing field due to the CMR of manganites. For low temperatures (T=2K), see Fig 8, the same anisotropic MR remains but a new in-plane peak (the pMR) arises and is enhanced by a magnetic field. In these figures, the top and bottom panels correspond to the two different current configurations $I_{[100]}$ and $I_{[010]}$ with the same qualitative behavior.

C. X-ray linear dichroism

To further investigate the interfacial electronic structure of the LSMO layers we have measured the x-ray linear dichroism (XLD) at the Mn $L_{2,3}$ edge of a series of superlattices with fixed thickness of the STO layer (2 unit cells) and 4, 6 and 14 unit cells LSMO layer. XLD, or natural dichroism, is the difference in the x ray absorption spectra (XAS) of horizontally and vertically linearly polarized x rays (with respect to sample surface). The $L_{2,3}$ XAS signal measures the excitation of electrons from a 2p state to an empty 3d state (an e_g orbital in the case of LSMO) and thus, the XLD signal is a chemically selective qualitative probe of orbital polarization. Positive (negative) values of the XLD signal reveal a preferential occupation of the in plane $d_{x^2-y^2}$ (out of plane $d_{3z^2-r^2}$) Mn e_g orbitals. Figures 9 (a) and (b) show the XAS signal normalized to the active volume of the (a) $[LSMO_{14}/STO_2]_8$ and (b) $[LSMO_4/STO_2]_8$ superlattices obtained with horizontal (black line) and vertical

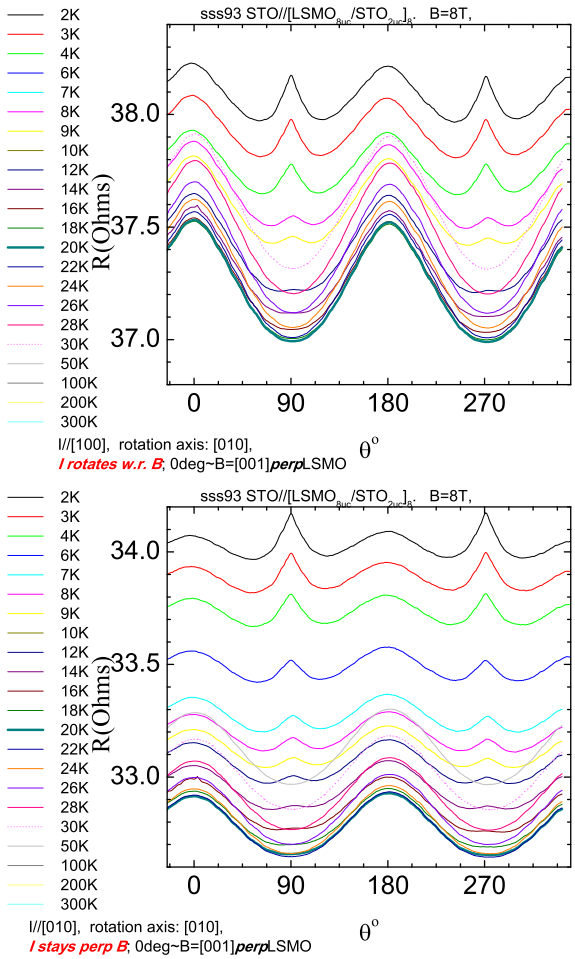

FIG. 6: (Color online) Angular magnetoresistance of a $[LSMO_8/STO_2]_8$ multilayer in 8 T magnetic field at various temperatures with (a) $I_{[100]}$ and (b) $I_{[010]}$ current geometries.

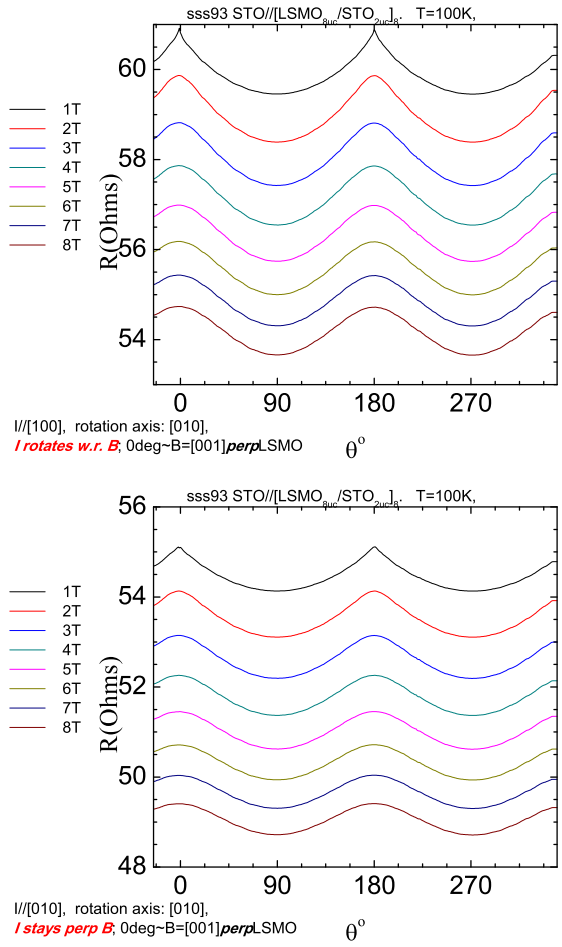

FIG. 7: (Color online) Angular magnetoresistance of a $[LSMO_8/STO_2]_8$ multilayer at T=100 K, in various magnetic fields, with (a) $I_{[100]}$ and (b) $I_{[010]}$ current geometries.

(red line) polarized x rays. The shape of the normalized XAS spectra (see insets) evidences a different degree of orbital polarization for the two samples. This is better observed in Fig. 9 (c), showing the XLD spectra of the $[LSMO_{14}/STO_2]_8$ (black line), $[LSMO_6/STO_2]_8$ (blue line) and $[LSMO_4/STO_2]_8$ (red line) superlattices. Notice that the XLD signals for the $[LSMO_{14}/STO_2]_8$ and $[LSMO_4/STO_2]_8$ superlattices have been obtained from the XAS measurements showed in Figs 9 (a) and (b). Interestingly, the decrease in the manganite layer thickness is accompanied by an increase of the positive XLD signal. Since by decreasing the LSMO layer thickness the XLD measurement becomes more sensitive to the interface, this behaviour could be suggesting a change in the orbital polarization of the interfacial Mn e_g electrons, which become more $d_{x^2-y^2}$ polarized in the case of the $[LSMO_4/STO_2]_8$ superlattice. We can not rule out another possible contributions to changes observed in the XLD spectra. To ensure a minimum contribution of the ferromagnetic polarization of the Mn e_g spins to the XLD signal, the XAS was measured at room temperature and without applied magnetic field.

II. THEORY

A. Manganites model description

We describe the manganites within the spinless double exchange model that assumes an infinite Hund's coupling between the localized electrons on the t_{2g} orbitals and the itinerant ones on the e_g orbitals. The Hamiltonian is[12]

$$H = -\sum_{\langle mn\rangle\alpha\beta} t_{mn}^{\alpha\beta} c_{m\alpha}^{\dagger} c_{n\beta} + H_{\rm SO} \qquad (1)$$

where $c_{m\alpha}^{\dagger}$ creates an electron on the orbital α on the site m and $\langle mn\rangle$ means hoppings $t_{mn}^{\alpha\beta}$ are considered only to nearest neighbors. The orbital and direction dependent hoppings are $t^{x,y}_{3z^2-r^2,3z^2-r^2} = 1/4t$, $t^{z}_{3z^2-r^2,3z^2-r^2} = t$, $t^{x,y}_{x^2-y^2,x^2-y^2} = 3/4t$, $t^{z}_{x^2-y^2,x^2-y^2} = 0$, $t^{x}_{x^2-y^2,3z^2-r^2} =$

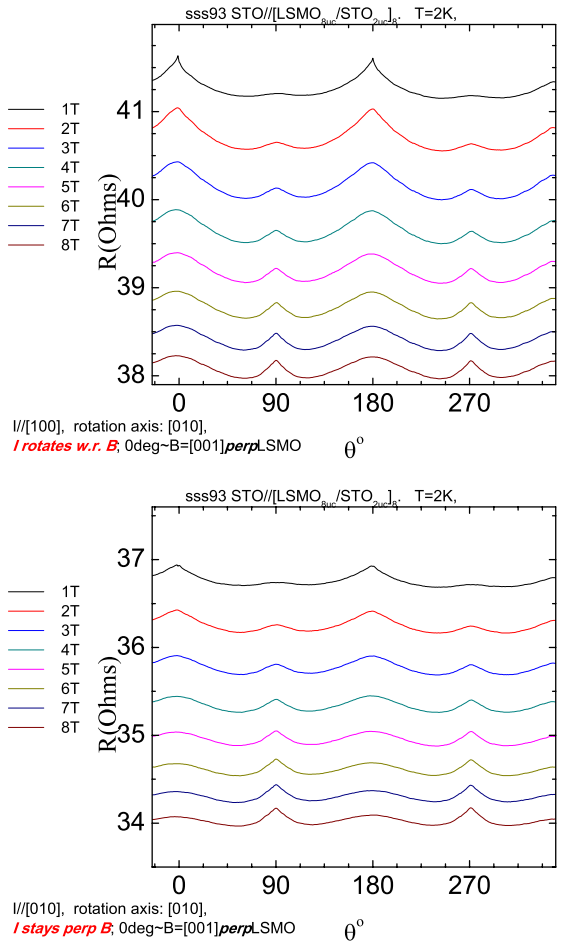

FIG. 8: (Color online) Angular magnetoresistance of a $[LSMO_8/STO_2]_8$ multilayer at T=2 K, in various magnetic fields, with (a) $I_{[100]}$ and (b) $I_{[010]}$ current geometries.

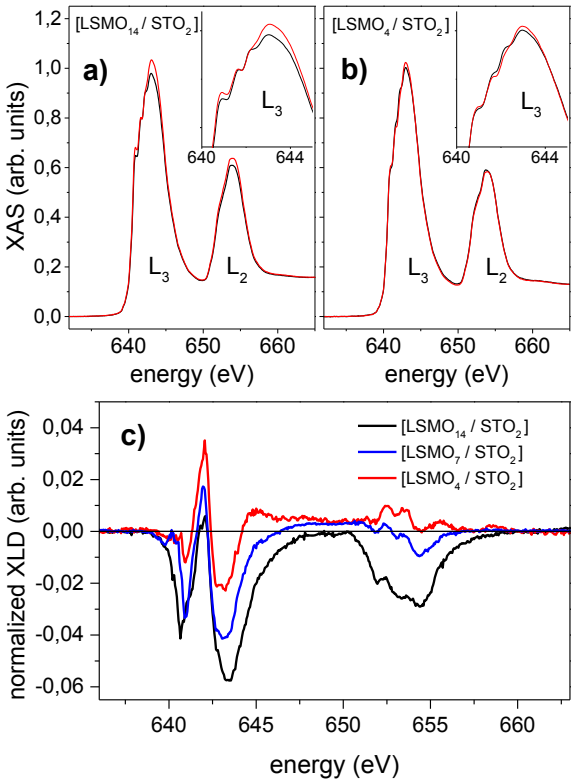

FIG. 9: (Color online) XAS signal of the (a) $[LSMO_{14}/STO_2]_8$ and (b) $[LSMO_4/STO_2]_8$ superlattices obtained with vertical (black) and horizontal (red) linearly polarized x-rays (with respect to sample surface). The signals were measured at room temperature and without applied magnetic field. The insets in both figures are zooms of the L_3 peaks to better observe the differences when the beam polarization is changed. (c) XLD signal (vertical minus horizontal) of $[LSMO_{14}/STO_2]_8$ (black), $[LSMO_6/STO_2]_8$ (blue) and $[LSMO_4/STO_2]_8$ (red) superlattices. A systematic increase of the positive area of the signal can be observed with the increase of the sensitivity to the interfacial Mn as the thickness of the manganite layer is reduced.

$t^y_{x^2-y^2,3z^2-r^2} = \sqrt{3}/4t$, $t^z_{x^2-y^2,3z^2-r^2} = 0$, with t the energy unit. There is no direct spin-orbit coupling between the e_g orbitals but they are coupled through the t_{2g} ones. From second order perturbation theory,

$$H_{\rm SO} = g \begin{pmatrix} 3\sin^2(\theta) & \sqrt{3}\sin^2(\theta)\cos(2\phi) \\ \sqrt{3}\sin^2(\theta)\cos(2\phi) & \sin^2(\theta)+4\cos^2(\theta) \end{pmatrix}$$

where $g = \lambda^2/\Delta$, with λ the spin-orbit coupling and Δ the crystal field splitting between the e_g and the t_{2g} orbitals. $H_{\rm SO}(1,1)$ refers to the $3z^2-r^2$ orbital. θ and ϕ give the orientation of the magnetization (or the external magnetic field) in spherical coordinates (namely, θ is the out-of-plane angle and ϕ is the rotation within the plane). Note that $H_{\rm SO}$ only depends on the orientation and not on the intensity of the applied magnetic field.

The Hamiltonian is solved for different values of the magnetic field orientation and the resulting bands used to calculate the conductivity with

$$\sigma_{ij} = e^2\tau \sum_n \int d\mathbf{k}\, \frac{\partial f(\epsilon)}{\partial \epsilon_n(\mathbf{k})}\, v^i_n(\mathbf{k}) v^j_n(\mathbf{k}) \qquad (2)$$

The result depends neither on the magnetic field intensity nor on the temperature as a fully saturated magnetization is always considered.

Within this model, both the in-plane and out-of-plane anisotropic MR are accounted for. For an in-plane applied magnetic field, the variation of ϕ (the relative angle between the current and B) changes the sign of the $\langle x^2-y^2|H_{\rm SO}|3z^2-r^2\rangle$ term breaking the $x-y$ symmetry of the bands[12]. The out-of-plane anisotropic MR is accounted for by the $H_{\rm SO}$ dependence on θ.

The different qualitative behaviour of $\rho(\theta)$ for a 2D and a 3D manganite is reflected on some distinct features in the bands, shown in Figs. 10 and 11. The first thing to note is that the 2D system splits the e_g orbitals pushing up the $3z^2-r^2$ one. Therefore, the x^2-y^2 occupation is larger. However, transport properties are dominated by the bands around the Fermi energy. In the 2D case, the dominant orbital in terms of transport is $3z^2-r^2$. An analysis of the spin-orbit coupling term shows that the onsite energy on the $3z^2-r^2$ orbital increases with θ from 0 (out-of-plane) to $\pi/2$ (in-plane). This produces the effect of narrowing the band around the Γ point, leading to a decreasing velocity (increasing resisitivity) for $\theta=\pi/2$. The opposite effect is produced on the x^2-y^2 orbital but the corresponding band does not participate in transport at $x=0.3$. The critical x separating the $3z^2-r^2$ and the x^2-y^2 dominated transport is around $x=0.5$.

The 3D case is completely different as shown in Fig. 11. Here the two e_g orbitals are roughly equally populated at all energies. Therefore the behaviour of the resistivity is the same as the one expected in the naive parabolic band picture.

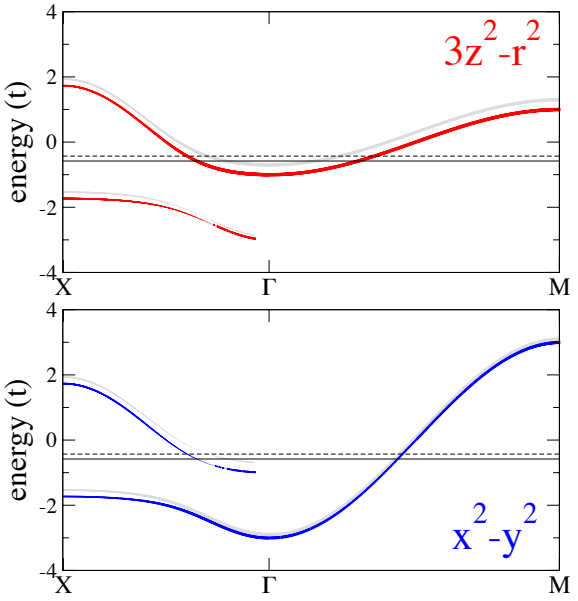

FIG. 10: (Color online) Manganite 2D bands weighted on the $3z^2-r^2$ (top) and the x^2-y^2 (bottom) orbitals in the presence of spin-orbit coupling. A fairly large value of this coupling is considered ($g=0.1t$) in order to see the effect. The dark bands correspond to a perpendicular magnetic field $\theta=0$ and the light ones to an in-plane magnetic field $\theta=\pi/2$. ϕ, the orientation of the field within the plane, is chosen to be $\pi/4$ in order to get isotropic bands in the $x-y$ plane and allow us to focus on the effect of θ. The horizontal lines mark the position of the Fermi level corresponding to $x=0.3$: the solid line for $\theta=0$ and the dashed line for $\theta=\pi/2$. Note that the $3z^2-r^2$ orbital is much more dominant than the x^2-y^2 one at the Fermi level (there is a factor of 3 in relative occupation. Looking at the parabolic-like band around the Γ point, it is visible that the derivative of the bands with respect to k (velocity) decreases when the magnetic field rotates from an out-of-plane to an in-plane configuration. A decrease in velocity implies an increase in resistivity (see Eq. 2).

B. Spin-orbit coupling on the $SrTiO_3$ interface

A 2D gas could be forming on the $SrTiO_3$ interface, similar to the one forming on the $LaAlO_3/SrTiO_3$ heterostructures. In these heterostructures, similar transport measurements have shown an out-of-plane peak on the resistivity and a minimum for an in-plane field. We get theoretically the same qualitative result for the resistivity (Fig. 4(b) in the main text). The t_{2g} orbitals are split in a two-dimensional gas[13] such that xy is shifted down with respect to zx and yz. As the charge in the STO is small, it is reasonable to assume only the xy band is occupied. We therefore consider a 1-band system with Rashba spin-orbit coupling within effective mass

$$H=\frac{\hbar^2(k_x^2+k_y^2)}{2m^*}+\alpha_{\rm SO}(\sigma_x k_y-\sigma_y k_x)$$

under an applied magnetic field $\vec{H}\vec{\sigma}$. $m^*=0.41m_e$ and $\alpha_{\rm SO}=0.0076$ eV Å.[14]

C. Density functional theory calculations

The DFT+U calculations use PAW pseudopotentials, a plane wave expansion kinetic-energy cutoff of 400 eV and a regular $\Gamma-$centered $9\times9\times1$ k-point mesh in the Brillouin zone. The O(2s), Ti(3s,3p), Sr(4s,4p), La(5s,5p) and Mn(3s,3p) semicore states are included as valence electrons. A repulsive on-site Coulomb interaction following the Dudarev approach is added to avoid the self-interaction errors[15]. The Coulomb U and exchange J parameters are taken as 8.5 and 0.5 for d Ti and 2.5 and 0.5 eV, respectively for d Mn[16]. Geometries were relaxed employing a conjugate gradient algorithm until the forces on all atoms were less than 0.01 eV/Å.

We performed calculations for $LSMO_m/STO_n$ superlattices (SLs) with $6.5\leq m\leq14.5$ and $2.5\leq n\leq7.5$. The LSMO alloy is modeled by a 1×1 ordered alloy containing two LaO and a SrO planes in each LSMO u.c. The crystal structure of the SLs is tetragonal and we fix the in-plane lattice constant to the experimental value 3.905 Å, which is equal to the bulk STO lattice parameter and almost identical to the calculated equilibrium STO 3.899 Å. Full structural optimization was performed to obtain the out-of-plane $c-$axis lattice constant as well as the internal atomic positions within the cell.

For a uniform composition of the LSMO layer, the SL ground state is metallic and a uniform ferromagnetic coupling between neighboring Mn planes is stabilized. The partially occupied Mn-e_g states mediate the strong Zener double exchange and promote the ferromagnetic order.

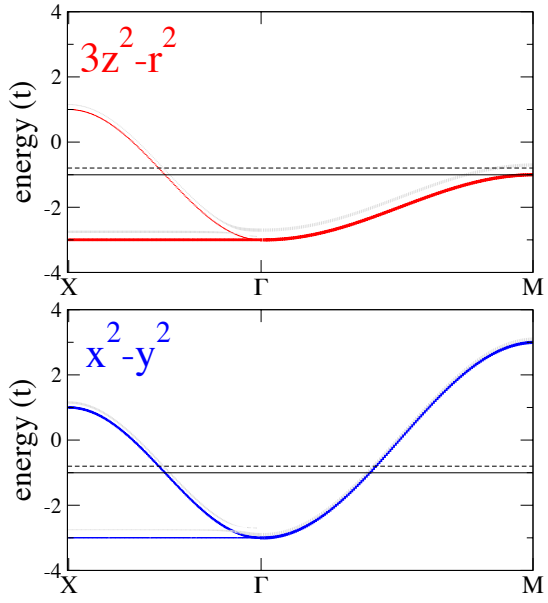

FIG. 11: (Color online) Same as Fig. 10 for a 3D manganite. In this case, the bands at the Fermi level are equally occupied by both orbitals and the modification of the bands with θ is less noticeable.

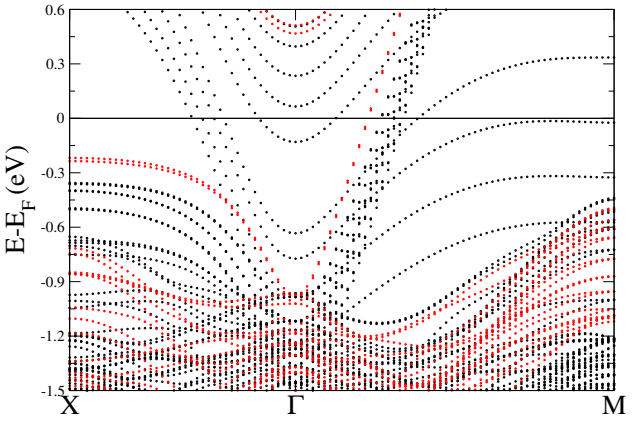

FIG. 12: (Color online) Calculated band structure of the $LSMO_{14.5}/STO_{2.5}$ superlattice along the high symmetry directions of the SL BZ. Black and red (grey) circles correspond to majority and minority spin bands, respectively.

The calculated magnetic moments of the Mn atoms are $\sim 3.5\mu_B$, consistent with the nominal $t_{2g}^3 e_g^{0.7}$ occupancy, and almost independent of the Mn location within the LSMO slab.

However, a two-layer model seems to be more appropriate for the system at hand. The slab is composed of a stoichiometric LSMO bulk-like central layer and two interface layers with a different stoichiometry, containing two MnO_2 planes. These layers may account for local structural or chemical disorder, intermixing, etc. We made calculations for several stoichiometries at the interface layer and found that in the relaxed structures, for most cases, the FM alignment of the interface Mn planes is lower in energy than the AFM alignment. However, for a Sr-rich interface the AFM coupling is most favorable. Note that the LSMO bulk phase diagram[17] shows an A-type antiferromagnetic phase for $x > 0.5$.

The calculated band structure for the $LSMO_{14.5}/STO_{2.5}$ SL is displayed in Fig.12. The uppermost filled Mn e_g bands, with energies in the region 1 eV below E_F, exhibit majority spin orientation except two bands with opposite spin, which are spatially localized in the interface MnO_2 planes. For lower energies, Mn t_{2g} states are strongly entangled with Op-like and STO derived valence bands.

[1] J.-L. Maurice, D. Imhoff, J.-P. Contour, and C. Colliex, Philosophical Magazine **86**, 2127 (2006).

[2] M. Yoshimoto, H. Maruta, T. Ohnishi, K. Sasaki, and H. Koinuma, Applied Physics Letters **73**, 187 (1998).

[3] H. Boschker, J. Verbeeck, R. Egoavil, S. Bals, G. van Tendeloo, M. Huijben, E. P. Houwman, G. Koster, D. H. A. Blank, and G. Rijnders, Advanced Functional Materials **22**, 2235 (2012), ISSN 1616-3028.

[4] A. Y. Petrov, X. Torrelles, A. Verna, H. Xu, A. Cossaro, M. Pedio, J. Garcia-Barriocanal, G. R. Castro, and B. A. Davidson, Advanced Materials **25**, 4043 (2013).

[5] F. Y. Bruno, J. Garcia-Barriocanal, M. Varela, N. M. Nemes, P. Thakur, J. C. Cezar, N. B. Brookes, A. Rivera-Calzada, M. Garcia-Hernandez, C. Leon, et al., Physical Review Letters **106**, 147205 (2011).

[6] J. Garcia-Barriocanal, F. Y. Bruno, A. Rivera-Calzada, Z. Sefrioui, N. M. Nemes, M. Garcia-Hernandez, J. Rubio-Zuazo, G. R. Castro, M. Varela, S. J. Pennycook, et al., ADVANCED MATERIALS **22**, 627 (2010).

[7] C. Visani, J. Tornos, N. M. Nemes, M. Rocci, C. Leon, J. Santamaria, S. G. E. te Velthuis, Y. Liu, A. Hoffmann, J. W. Freeland, et al., Phys. Rev. B **84**, 060405 (2011).

[8] J. Garcia-Barriocanal, A. M. Perez-Muñoz, Z. Sefrioui, D. Arias, M. Varela, C. Leon, S. J. Pennycook, and J. Santamaria, Phys. Rev. B **87**, 245105 (2013).

[9] J. Garcia-Barriocanal, A. Rivera-Calzada, M. Varela, Z. Sefrioui, E. Iborra, C. Leon, S. J. Pennycook, and J. Santamaria, Science **321**, 676 (2008), http://www.sciencemag.org/content/321/5889/676.full.pdf, URL `http://www.sciencemag.org/content/321/5889/676.abstract`.

[10] L. Maritato, C. Adamo, C. Barone, G. De Luca, A. Galdi, P. Orgiani, and A. Petrov, Phys. Rev. B **73** (2006), ISSN 1098-0121.

[11] M. Bibes, V. Laukhin, S. Valencia, B. Martinez, J. Fontcuberta, O. Gorbenko, A. Kaul, and J. Martinez, Journal of Physics - Condensed Matter **17**, 2733 (2005).

[12] J. D. Fuhr, M. Granada, L. B. Steren, and B. Alascio, Journal of Physics Condensed Matter **22**, 146001 (2010).

[13] A. Santander-Syro, O. Copie, T. Kondo, F. Fortuna, S. Pailhs, R. Weht, X. Qiu, F. Bertran, A. Nicolaou, A. Taleb-Ibrahimi, et al., Nature **469**, 189 (2011).

[14] Z. Zhong, A. Tóth, and K. Held, Phys. Rev. B **87**, 161102 (2013).

[15] S. Dudarev, G. Botton, S. Y. Savrasov, C. Humphreys, and A. Sutton, Phys. Rev. B **57**, 1505 (1998).

[16] L. Y. Chen, C. Le Chen, K. X. Jin, S. F. Wang, and X. Du, Phys. Status Solidi (b) **250**, 402 (2013).

[17] Y. Tokura, Rep. Prog. Phys. **69**, 797 (2006).